Simulation of Ship Propeller Load Based on MRASO-MPTC Control

Li Gang

Sichuan Geely University, Jianyang City, 641423 Chengdu, China
ligangdzxxgc@bgu.edu.cn

Abstract: In this paper, a sensorless control strategy using Permanent Magnet Synchronous Motor (PMSM) based on Model Reference Adaptive System Observer (MRASO) is designed. The Model Predictive Torque Control (MPTC) system of PMSM driven by Matrix Converter (MC) is analyzed and studied in an indirect way. Different from the traditional control strategy, this paper proposes a scheme that the MC is equivalent to the combination of two topologies: virtual DC-AC converter and virtual AC-DC converter. MPTC is proposed to select the voltage vector of the virtual DC-AC converter to solve the problem of large torque ripple and flux ripple. The hysteresis comparator is used to select the current vector of the virtual AC-DC converter, so that the Power Factor (PF) at the input side is 1. Through different combinations of voltage vector and current vector, the MC is in different switching states, so as to realize the control of PMSM system. Through the simulation of the propeller system, the feasibility of PMSM for mechanical load and propeller load simulation is verified, and the effectiveness of MRASO-MPTC control strategy for propeller load simulation is verified.

Keywords: Ship propeller load, PMSM, MC, MRASO-MPTC, Simulation.

1. Introduction

The electrical load simulation technology consists of using the DC motor or AC motor as the load equipment, real-time control of motor torque, and load it on the bearing equipment, in order to achieve the purpose of load simulation. PMSM has significant advantages in efficiency, power density, speed control performance, dynamic performance, maintenance and environmental protection, and has been widely used in many fields (Wang et al., 2023).

As a key propulsion component of a ship, the performance of a propeller directly determines the sailing speed, mobility and energy efficiency of a ship. By simulating and controlling the operation of the propeller under different load conditions, the design parameters of the propeller (such as blade shape, pitch angle, etc.) can be optimized, so as to improve the overall propulsion efficiency and performance. In practice, propellers may encounter a variety of complex and variable working conditions, including different speeds, depths, flow conditions, and sudden load changes. Performing load simulation control studies can help predict and simulate the propeller performance under these extreme conditions, ensuring that it can operate stably under various conditions, thereby improving the reliability and durability of the overall system. So, it is urgent to carry out the control research of ship propeller load simulation (Oral & Akay, 2022).

Sensorless control technology refers to the accurate monitoring and control of PMSM running state through algorithms and signal processing methods, without additional physical sensors (Taghinezhad Vaskeh Mahaleh et al., 2024).

Kulikova & Kulikov (2024) proposed an observer-based control to integrate the observer into the control system: the designed observer is combined with the propeller load simulation system to form a closed-loop control system. The observer is responsible for estimating the system state and provides these estimates to the controller as feedback. However, observer-based control heavily depends on the accuracy of the system model. If the mathematical model of the propeller load has errors or fails to adequately capture all key dynamic characteristics such as high nonlinearity, complex coupling, etc., the performance of the observer will be severely affected, leading to inaccurate state estimation. Some advanced observers, such as Extended Kalman Filter, Sliding Mode Observer, etc., may be computationally complex and require high computational resources. In real-time control systems, this may lead to slow response or fail to meet real-time requirements (Kulikova & Kulikov, 2024).

Tomov et al. (2022) proposed an Adaptive Control, which uses an Adaptive Control Algorithm to dynamically adjust the internal model parameters of the load simulator according to real-time measurement data (such as propeller speed, thrust, torque, etc.) to ensure that the model can accurately reflect the load characteristics of the propeller

under different working conditions. However, due to the complexity of the adaptive control algorithm, its debugging and optimization process may be cumbersome. Inappropriate parameter settings or algorithm implementation errors may lead to system performance degradation or even instability (Tomov et al., 2022).

Espinoza Fraireet et al. (2024) presented a Nonlinear Control. Ship propeller and load simulation system often have strong nonlinear characteristics. Nonlinear control strategy can directly model and control design for these characteristics, so as to describe and deal with the dynamic changes of the system more accurately. But the design of nonlinear controllers usually relies on accurate mathematical models which require a deep understanding and accurate description of the nonlinear characteristics of the system. However, the nonlinear characteristics of ship propellers and their load systems are often complex and variable, being difficult to fully capture by simple mathematical models (Espinoza Fraireet et al., 2024).

Model Predictive Control (MPC) originated in the 1970s and was originally mainly aimed at solving optimal control problems for linear systems (Agyeman et al., 2024).

In order to improve the performance of the motor current loop, Liu et al. (2023)designed a beatless discrete current predictive control strategy. The main idea is to use the desired current value and the feedback current value to calculate the voltage vector, and convert it into the switching signal under the spatial pulse width modulation module. The robust current prediction algorithm is introduced to effectively control the parameter error of the model prediction. However, this approach relies on an accurate system model. If the model is inaccurate, the control performance may be severely affected.

Based on the feedback of the input and output ports to the system, Madalin Costin et al. used linear control to decouple the system and used iterative quadratic programming method to solve the problem of non-convergence of feasible solutions caused by nonlinear constraints (Madalin Costin & Corneliu Lazar, 2024). Even though, this method is extremely sensitive to the initial value, and the solution of iterative quadratic

programming method may be affected by the initial value. If the initial value is not chosen properly, the algorithm may fall into a local optimal solution.

In order to simplify the calculation process of MPC, Tarbajovsky et al. (2023) linearized the nonlinear PMSM model based on input-output lines to avoid solving nonlinear constrained optimization problems. However, for the PMSM model with strong nonlinearity, especially when the operating point is far away from the linearization point, the linearization may lead to the degradation of the control performance.

Based on the problems existing in the previous research, this paper will take PMSM as the load motor, design a control method based on MRASO-MPTC, use the MATLAB/Simulink simulation environment, combined with the propeller load characteristics, build the simulation model of the propeller load simulation system, and carry out simulation research on the system. The simulation results are analysed and explained to solve the existing problems.

Section 2 introduces the PMSM mathematical model and redesigns the MRASO to select the voltage space vector of the MPTC while selecting the current space vector of the hysteresis comparator. In Section 3, the corresponding simulation analysis is made for the direct navigation of the ship, the hierarchical start, the reverse process after the ship's forward start, and the stop process after the ship's forward start. In Section 4, the control effect of adopting MRASO-MPTC strategy is discussed, and the optimal choice of adopting mode in the process of ship starting and stopping is obtained.

2. Design of Ship Propeller Load System Mathematical Model

Figure 1 shows the ship propeller load motor simulation system, which is mainly composed of the following parts: propeller model, PMSM, MC, MRASO, voltage space vector selection based on MPTC, current space vector selection based on hysteresis comparator, and MC switching state table. In this paper, the model predictive controller is used to predict the flux and torque at the next sampling time, and then the output side control voltage vector U_o is selected by evaluating the
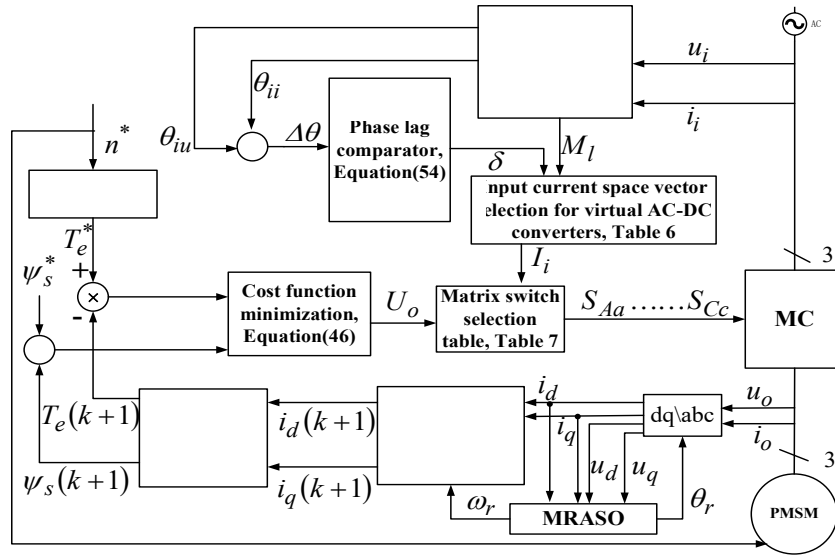
Figure 1. Simulation system of ship propeller load motor

defined cost function. MC adjusts the input side vector through the on-off closure of the switching element and picks out the current vector I_i that can ensure that the phase difference between the input voltage and the input current vector is zero. U_o and I_i jointly adjust the switching state of the MC to complete the control of the PMSM speed and flux.

2.1 PMSM Mathematical Model

PMSM is a nonlinear, multivariate and strongly coupled complex system (Popovici & Onea, 2021). Ignoring the effects of core saturation, hysteresis loss and eddy current loss of permanent magnet synchronous motor, and because the surface mounted PMSM is taken as the research object in this paper, and the stator inductance $L_d = L_q = L$, the dynamic mathematical model under the d-q coordinate system is as follows:

$$\begin{cases} \dfrac{di_d}{dt} = -\dfrac{R}{L}i_d + \omega_r i_q + \dfrac{u_d}{L} \\ \dfrac{di_q}{dt} = -\dfrac{R}{L}i_q - \omega_r i_d - \dfrac{\psi_f}{L}\omega_r + \dfrac{u_q}{L} \end{cases} \quad (1)$$

where i_d, i_q, u_d and u_q are the stator current and stator voltage in d-q coordinate system respectively. ω_r, R, and Ψ_f are the electrical angular speed, stator resistance, and rotor permanent magnet flux, respectively.

The stator flux equation is as follows:

$$\begin{cases} \psi_d = L i_d + \psi_f \\ \psi_q = L i_q \end{cases} \quad (2)$$

where Ψ_d and Ψ_q are the flux components corresponding to the d-axis and q-axis, respectively.

The electromagnetic torque equation is the following.

$$T_e = 1.5 p i_q \psi_f \quad (3)$$

where T_e and p are electromagnetic torque and number of poles, respectively.

2.2 The Design of MRASO

According to the MRASO principle (Saihi et al., 2023), the PMSM dynamic mathematical model is set up with reference model and adjustable model. First, let:

$$\begin{cases} i_d^{'} = i_d + \dfrac{\psi_f}{L} \\ i_q^{'} = i_q \\ u_d^{'} = u_d + \dfrac{R\psi_f}{L} \\ u_q^{'} = u_q \end{cases} \quad (4)$$

The reference model is set according to equation (1), and is expressed as follows:

$$\begin{bmatrix} \dfrac{di_d^{'}}{dt} \\ \dfrac{di_q^{'}}{dt} \end{bmatrix} = \begin{bmatrix} -\dfrac{R}{L} & \omega_r \\ -\omega_e & -\dfrac{R}{L} \end{bmatrix} \begin{bmatrix} i_d^{'} \\ i_q^{'} \end{bmatrix} + \begin{bmatrix} \dfrac{1}{L} & 0 \\ 0 & \dfrac{1}{L} \end{bmatrix} \begin{bmatrix} u_d^{'} \\ u_q^{'} \end{bmatrix} \quad (5)$$

Meanwhile, according to equation (5), the adjustable model setting is the following:

$$\begin{bmatrix} \dfrac{d\hat{i'_d}}{dt} \\ \dfrac{d\hat{i'_q}}{dt} \end{bmatrix} = \begin{bmatrix} -\dfrac{R}{L} & \hat{\omega}_r \\ -\hat{\omega}_r & -\dfrac{R}{L} \end{bmatrix}\begin{bmatrix} \hat{i'_d} \\ \hat{i'_q} \end{bmatrix} + \begin{bmatrix} \dfrac{1}{L} & 0 \\ 0 & \dfrac{1}{L} \end{bmatrix}\begin{bmatrix} u'_d \\ u'_q \end{bmatrix} \quad (6)$$

where the variable with "^" represents the corresponding estimated value.

By subtracting Equations (5) and (6), the following can be obtained.

$$\begin{bmatrix} \dfrac{d}{dt}\tilde{i'_d} \\ \dfrac{d}{dt}\tilde{i'_q} \end{bmatrix} = \begin{bmatrix} -\dfrac{R}{L} & \omega_r \\ -\omega_r & -\dfrac{R}{L} \end{bmatrix}\begin{bmatrix} \tilde{i'_d} \\ \tilde{i'_q} \end{bmatrix} + \begin{bmatrix} 0 & \tilde{u}_r \\ \tilde{\tilde{u}}_r & 0 \end{bmatrix}\begin{bmatrix} \hat{i'_d} \\ \hat{i'_q} \end{bmatrix} \quad (7)$$

Where, the variable with "Δ" represents the difference between the reference value and the estimated value.

Rewrite Equation (7) as follows:

$$\frac{d}{dt}\tilde{i'_s} = -F\,\tilde{i'_s} - G \quad (8)$$

where $F = \begin{bmatrix} -\dfrac{R}{L} & \omega_r \\ -\omega_r & -\dfrac{R}{L} \end{bmatrix}$, $G = \begin{bmatrix} 0 & \tilde{u}_r \\ -\tilde{\tilde{u}}_r & 0 \end{bmatrix}\begin{bmatrix} \hat{i'_d} \\ \hat{i'_q} \end{bmatrix}$.

According to Popov's hyperstability theory (Nikitin et al., 2023), to make the system stable, the estimated speed ω_r and rotor position θ_r should be expressed as follows:

$$\begin{cases} \hat{\omega}_r = \left[K_p + \dfrac{K_i}{s} \right]\left[i_d\hat{i}_q - i_q\hat{i}_d - \dfrac{\psi_f}{L}\left(i_q - \hat{i}_q \right) \right] \\ \hat{\theta}_r = \int \hat{\omega}_r\, dt \end{cases} \quad (9)$$

2.3 MPTC-based Voltage Space Vector Selection

The Euler discretization (Esquível & Krasii, 2020) of Equation (1) can be used to calculate the current prediction model shown in Equation (10):

$$\begin{cases} i_d(k+1) = T_s\dfrac{1}{L}\begin{bmatrix} u_d(k) - Ri_d(k) + \\ pL\omega_r(k)i_q(k) \end{bmatrix} + i_d(k) \\ i_q(k+1) = T_s\dfrac{1}{L}\begin{bmatrix} u_q(k) - Ri_q(k) - \\ p\omega_r(k)\left(Li_d(k) + \psi_f \right) \end{bmatrix} + i_q(k) \end{cases} \quad (10)$$

where T_s is the sampling time; k describes the kth sampling interval in discrete models.

The flux equation of equation (2) and the torque equation of equation (3) are respectively discretized by Euler, and the predicted flux and predicted torque are calculated, as shown in equations (11) and (12):

$$\psi_s(k+1) = \sqrt{\left(Li_d(k+1) + \psi_f \right)^2 + \left(Li_q(k+1) \right)^2} \quad (11)$$

$$T_e(k+1) = 1.5pi_q(k+1)\psi_f \quad (12)$$

For MPTC, the cost function that defines the model prediction is shown in Equation (13):

$$\begin{aligned} min. \quad & F = \left| T_e^* - T_e(k+1) \right| + B_1\left\| \psi_s^* \right| - \left| \psi_s(k+1) \right\| \\ s.t. \quad & U_i \in \{U_0, U_1, \ldots\ldots, U_7\}, i = 0,1,\ldots\ldots,7 \end{aligned} \quad (13)$$

where F is the cost function; T_e^* and ψ_s^* are the reference values of torque and flux, respectively; $T_e(k+1)$ and $\Psi_s(k+1)$ are the predicted values of torque and flux, respectively and B is the weight factor. In this paper, B_1 is chosen as T_n/Ψ_n (T_n and Ψ_n are the rated values of torque and stator flux, respectively). U_0, U_1,... , U_7 is the eight voltage vectors generated by the virtual DC-AC converter (where U_0 and U_7 are zero voltage vectors). Table 2 shows the output voltage space vector of the virtual DC-AC converter.

Table 2. Output voltage space vector of the virtual DC-AC converter

Voltage vector	S_A^k, S_B^k, S_C^k	Phase A	Phase B	Phase C
U_1	000	0	0	0
U_2	100	$2U_{dc}/3$	$-U_{dc}/3$	$-U_{dc}/3$
U_3	110	$U_{dc}/3$	$U_{dc}/3$	$-2U_{dc}/3$
U_4	010	$-U_{dc}/3$	$2U_{dc}/3$	$-U_{dc}/3$
U_5	011	$-2U_{dc}/3$	$U_{dc}/3$	$U_{dc}/3$
U_6	001	$-U_{dc}/3$	$-U_{dc}/3$	$2U_{dc}/3$
U_7	101	$U_{dc}/3$	$-2U_{dc}/3$	$U_{dc}/3$
U_8	111	0	0	0

At the k_{th} sampling time, the voltage vector U_i ($i=$ 0,1,2,... ., 7) satisfies equation (14):

$$U_i = 1.5U_d\left(S_A^k + S_B^k e^{j2\pi/3} + S_C^k e^{j4\pi/3} \right) \quad (14)$$

where U_{dc} represents DC bus voltage; S_i^k ($i=$A, B, C) is the state of the switch tube of the virtual DC-AC converter at kth sampling times and $S_i^k = 1$ (high level) and $S_i^k = 0$ (low level) indicate that the switch tube is on and off, respectively.

According to the MPTC principle (Arshad et al., 2023), the appropriate output voltage vector of virtual DC-AC converter can be picked out.

After each sampling period, the system will automatically generate an output voltage vector, and then the cost function value F corresponding to the voltage vector can be obtained through calculation. By comparing the cost function values generated by each sampling period, an optimal switching state of the converter can be obtained.

In order to maximize the electromagnetic torque of the system, the maximum torque current ratio is usually controlled. Figure 2 shows the stator current vector diagram of PMSM.
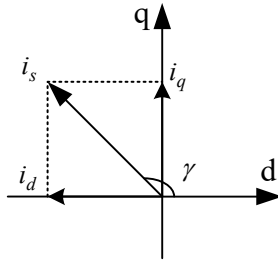
Figure 2. Stator current vector diagram of PMSM

According to Figure 2, it is obtained:

$$\begin{cases} i_d = i_s \cos\gamma \\ i_q = i_s \sin\gamma \end{cases} \tag{15}$$

Substituting Equation (15) into Equation (3), the following is obtained:

$$T_e = 1.5 p i_s \psi_f \sin\gamma \tag{16}$$

In order to achieve the maximum electromagnetic torque per unit current, it is necessary to meet:

$$\begin{cases} dT_e/d\gamma = 0 \\ d^2T_e/d^2\gamma < 0 \end{cases} \tag{17}$$

According to Equations (16) and (17), $\gamma=90°$, so the d-q axis reference current is the following:

$$\begin{cases} i_d^* = 0 \\ i_q^* = \dfrac{2}{3p\psi_f} T_e^* \end{cases} \tag{18}$$

The reference flux is:

$$\psi_s^* = \sqrt{\psi_f + \left(2 T_e^*/3p\psi_f\right)^2} \tag{19}$$

2.4 Current Space Vector Selection Based on Hysteresis Comparator

By comparing MC with the traditional AC-DC-AC converter, it can be found that the power supply voltage vector with adjustable PFMC input

side is the input side voltage vector. The difference between the input voltage space vector and the input current space vector consists in the phase property of being controllable or not. Conversely, the current vector is controlled by the switching state and the phase is controllable.

The MC is equivalent to a virtual AC-DC converter, which can make the input voltage and current vectors of the system have the same phase, and finally make the PF at the input side become 1. The magnitude phases of input voltage and current are θ_{iu} and θ_{ii}, respectively. After subtraction operation, the difference Δ_θ is sent to the hysteresis comparator, and then the sector $M_l (l=1,2,... ,6)$ to select the corresponding current vector.

The input current space vector of the virtual AC-DC converter is shown in Equation (20):

$$\begin{aligned} I_i &= \frac{2}{3} I_{dc} \left(S_a + S_b e^{j2\pi/3} + S_c e^{j4\pi/3} \right) \\ &= \frac{2}{3} \left(i_a + i_b e^{j2\pi/3} + i_c e^{j4\pi/3} \right) \end{aligned} \tag{20}$$

where I_{dc} is the DC current output of the virtual AC-DC converter. S_a, S_b and S_c indicate whether the circuit in directions a, b and c is on or not, respectively. "1" means that the upper bridge arm is conducting and the lower bridge arm is not conducting, "-1" means that the lower bridge arm is conducting and the upper bridge arm is not conducting, while "0" means that neither the upper bridge arm nor the lower bridge arm is conducting.

According to the analysis formula (20), the virtual AC-DC converter contains a total of nine input current space vectors $I_i (i=1\sim9)$, and the specific distribution is shown in Table 3.

Table 3. Input current space vector of the virtual AC-DC converter

Current vector	i_a	i_b	i_c	$S_{ap,}\ S_{bp,}\ S_{cp}$	$S_{an,}\ S_{bn,}\ S_{cn}$
I_1	I_{dc}	0	$-I_{dc}$	100	001
I_2	0	I_{dc}	$-I_{dc}$	010	001
I_3	$-I_{dc}$	I_{dc}	0	010	100
I_4	$-I_{dc}$	0	I_{dc}	001	100
I_5	0	$-I_{dc}$	I_{dc}	001	010
I_6	I_{dc}	$-I_{dc}$	0	100	010
I_7	0	0	0	100	100
I_8	0	0	0	010	010
I_9	0	0	0	001	001

In Table 3, S_{jk} ($j \in \{a,b,c\}$, $k \in \{p,n\}$) is the switching state of the virtual AC-DC converter, and $S_{jk}=1$ and $S_{jk}=0$ denote conduction and non-conduction, respectively. I_1 to I_6 are nonzero vectors, and I_7 to I_9 are zero vectors.

To select an optimal current vector, a phase hysteresis comparator should be used. The phase hysteresis comparator refers to the input of the difference Δ_θ to the hysteresis comparator, after the subtraction calculation of θ_{iu} and θ_{ii}, as shown in Figure 3.
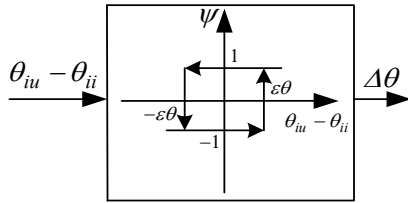
Figure 3. Schematic diagram of the phase hysteresis loop comparator

According to Figure 3, δ can be found by Equation (21):

$$\delta = \begin{cases} 1 & \theta_{iu} \text{-} \theta_{ii} = \Delta\theta > \varepsilon_\theta \\ \text{-}1 & \theta_{iu} \text{-} \theta_{ii} = \Delta\theta < \text{-}\varepsilon_\theta \end{cases} \qquad (21)$$

where ε_θ is the phase hysteresis comparator error bound.

According to Equation (21), when $\delta=1$, Δ_θ should be reduced, to slow down the phase variation of the leading input voltage vector. When $\delta=-1$, the same is true.

In order to effectively change the size of Δ_θ, the appropriate current vector must be selected in combination with the phase region of the voltage vector, to ensure that the phase difference between the input voltage and the current vector at the input side of the MC is 0. The selection of the switching state of the virtual DC-AC structure can be obtained as shown in Table 4, through which the appropriate current vector can be conveniently selected.

Table 4. Input current space vector selection for virtual AC-DC converter

| δ	M_1	M_2	M_3	M_4	M_5	M_6
1	I_1	I_2	I_3	I_4	I_5	I_6
-1	I_6	I_1	I_2	I_3	I_4	I_5

3. Simulation Analysis

From static state to straight sailing, there are two kinds of direct sailing methods commonly used by ships: direct sailing and graded sailing (Riaz et al., 2023). One can set the sail directly at a given propeller speed, so that the ship sails from a static state and at a steady speed, after reaching the given speed. Hierarchical sailing represents a hierarchical given speed: after the ship reaches the first level given speed and stabilizes, the given speed of the second level continues to increase until the speed stabilizes, and so on until the last level speed. The simulation of direct and hierarchical ship departure is carried out, respectively.

3.1 Simulation of the Ship's Direct Sailing Process

Direct start can make the propulsion motor reach the preset speed in a short time. If the propulsion motor starts for 10s, the propeller speed can also reach the set speed within 10s, because the propeller is directly connected to the propulsion motor. It is set that the motor starts after 20s of preheating and it takes 10s to reach the rated speed and maintain it.

The change curve of propeller speed and ship speed during direct start, from starting to steady state, is shown in Figure 4, and the change of torque during direct start is shown in Figure 5.
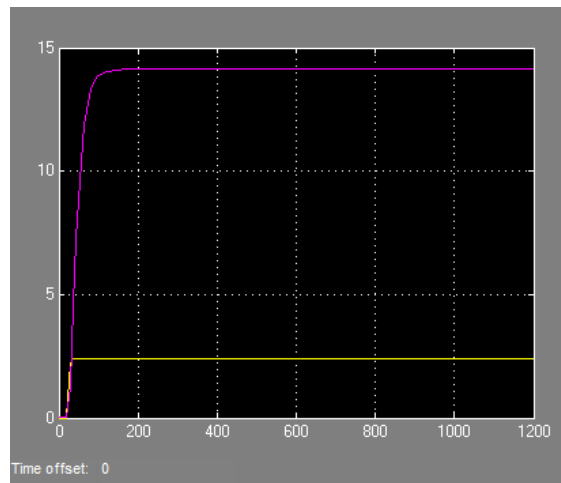
Figure 4. Response of ship speed v_s and paddle speed n during direct start
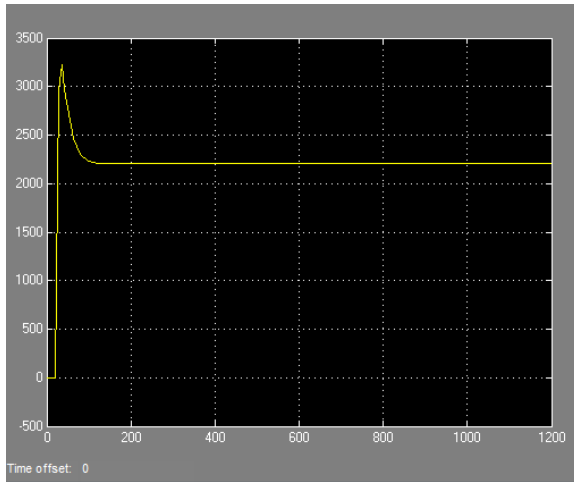
Figure 5. Response of propeller torque T_e when the ship is directly started

Figure 6. Response of ship speed v_s and paddle speed n during the graded start of the ship
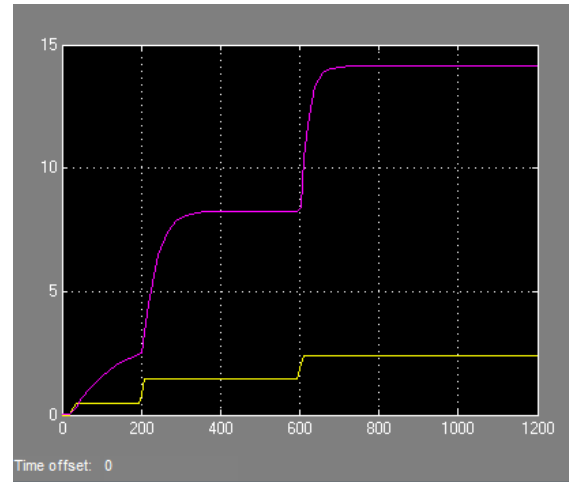
From Figures 4 and 5, it can be seen that the propeller speed and ship speed are 0 when the ship does not receive the sailing command at the beginning of the simulation. In 20s, the ship starts to set sail and reaches the maximum speed of 2.42r/s in 30s, which takes 10s. In this process, the torque also increases to the maximum value of 3203.8kNm. After that, the propeller speed stabilizes at 2.42r/s and the ship begins to accelerate, tending to be basically stable after 400s. The final speed of the ship is maintained at the maximum speed of 14.12m/s and the propeller torque begins to decrease gradually, after reaching the maximum value and being finally stabilized at 2202.7kNm.

In the simulation of the ship's direct forward start, the acceleration process of 10s will cause serious overload of the propeller shaft, and the damage caused by the equipment is great, which is not allowed in the actual operation of the ship.
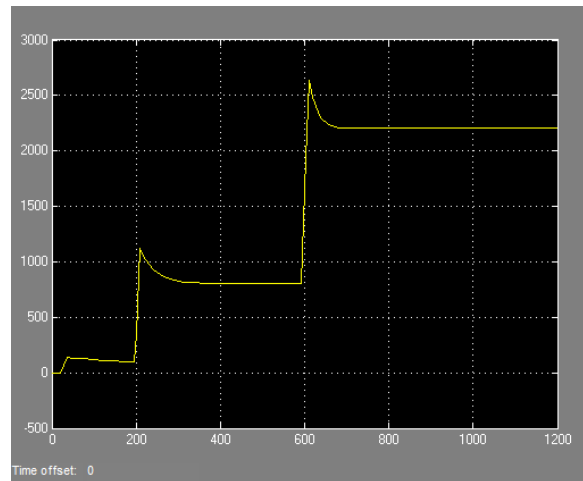
3.2 Simulation of the Ship's Graded Starting Process

The graded start can be divided into three stages: slow start acceleration, secondary acceleration and tertiary acceleration, so that the speed reaches the set rated speed step by step.

The change curve of propeller speed and ship speed from starting to steady state during the graded start is shown in Figure 6, and the change of torque during the graded start is shown in Figure 7.

Figure 7. Response of propeller torque T_e during the graded start of the ship

It can be seen from Figures 6 and 7 that before receiving the start signal in the first 20s, the ship remains stationary. At the beginning of the 20s simulation, the ship accelerates slowly to start, the propeller torque is small and the speed begins to increase. At 200s, the ship slows down the acceleration process, enters gradually into the low-speed stable sailing condition, and then the second stage of acceleration begins Within 5s, the propeller speed reaches 1.45r /s and the propeller torque increases to 806.5kNm. At 600s, the speed gradually tends to stabilise, the acceleration process slows down, and the torque begins to steadily decrease. At this time, the third stage of acceleration is carried out, and after 5s, the propeller reaches the maximum speed of 2.42r/s and the torque increases again, reaching the maximum value of 2702.2kNm. The ship also begins to accelerate and stabilises at the speed of 14.12m /s at 110s, which is the maximum speed of

the ship. The propeller torque begins to decrease from the maximum value and tends to stabilize at a value of 2203kNm, after 110s.

In the graded start, compared with the direct start, the propeller torque change is relatively small, the maximum torque is reduced by 501.6kNm, and there is no serious overload phenomenon in the graded start. Therefore, the actual ship start is all in this way.

3.3 Simulation of Reverse Process of the Ship After Starting the Forward Vehicle

In the actual operation of the ship, namely when the ship in the process of forward navigation, there will always be a variety of complex conditions. If there occurs a hazard in front of the helmsman or he is not sure about his safety, he often needs to slow down, reverse, or even stop the ship. When sailing through narrow channels, he also need to reverse the ship, in order to avoid the occurrence of collision accidents. Therefore, the study of this conditions can be used to obtain the motion characteristics of the ship when it is finally stable, at the maximum speed of reversal. Here, the dynamic process of the propeller rotation direction from positive to reverse and of the ship direction from forward to reverse is mainly analysed.

So, the ship runs under reverse condition, after starting the forward course. The change curves of propeller speed and ship speed, from the starting state to the steady state, are shown in Figure 8, and the change of torque during the whole process is shown in Figure 9.
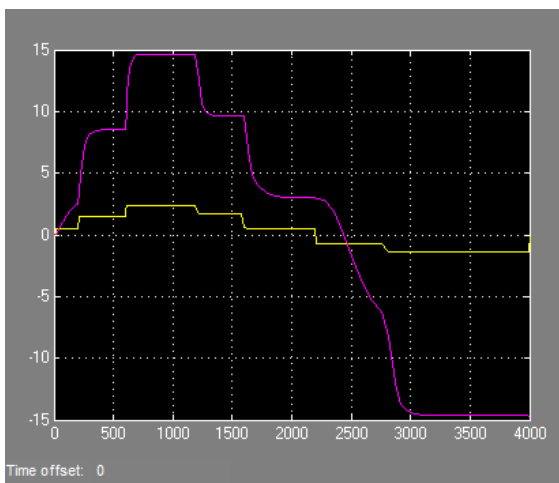
Figure 8. Response of the ship's reverse speed vs and paddle speed n after the ship's forward start
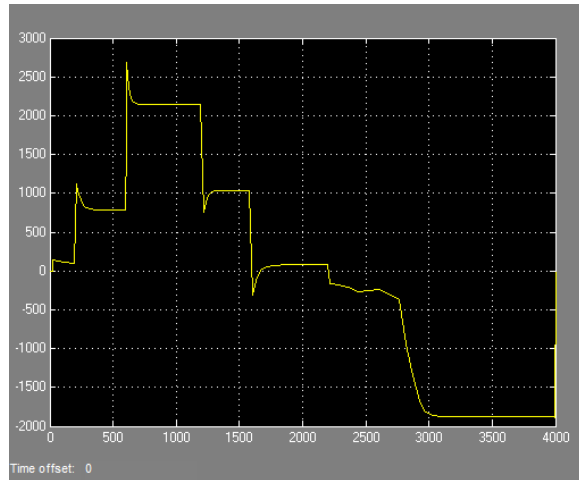
Figure 9. Response of reversing propeller torque T_e after the ship's forward start

From the simulation curves illustrated in Figures 8 and 9, it can be seen that, after the ship's forward course starts and after receiving the reverse signal at 1202s, the ship begins to slow down sails at a slower speed, after the second deceleration. The propeller speed changes from positive to negative at 2204s and, due to the inertia of the ship, the speed response is slow and the speed becomes negative at 2489s. That means that the ship starts to reverse. The propeller torque changes from a from positive value to a negative value at 1605s, and reaches the maximum reverse rotation speed of -1.38r/s at 2805s with the reverse acceleration of the propeller. The ship's reversing speed increases gradually, the maximum one being stabilized at -2.54m/s after 3000s, and the propeller torque remains at -2137kNm.

3.4 Simulation of the Stopping Process of the Ship After Starting the Forward Vehicle

After the beginning of the ship's graded starting process, the ship is slowed down in stages and the propeller speed is 0, as the main working condition of the simulation in this section, so that the actual operation condition of the ship when it stops sailing can be analysed.

So, the ship runs under stopping condition, after starting in normal course. The change curves of ship speed and propeller speed, from starting to final stopping, are shown in Figure 10 and the change of torque during the whole process is shown in Figure 11.
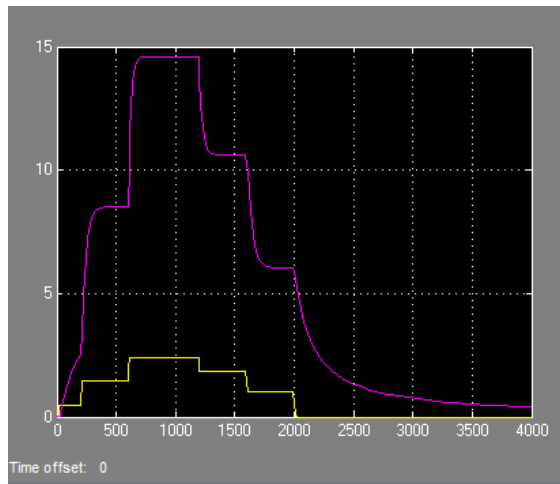
Figure 10. Response of stopping ship speed v_s and oar speed n after the ship's forward start
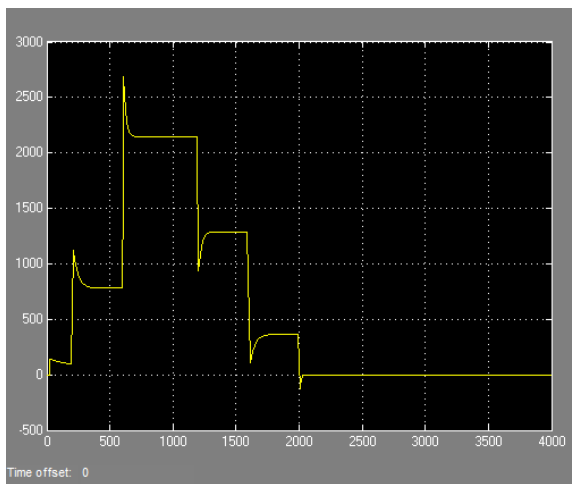
Figure 11. Response of the parking propeller torque T_e after the ship's forward start

From Figure 10, it can be seen that, after the second-level deceleration, the ship's speed was 5.78m/s in 2000s, and then the propeller speed became 0 within 10s, while the ship's speed continued to decrease, but it could not completely become 0. That is because the ship has a large self-weight, so the inertia is huge, and simply reducing the speed of the propulsion motor to 0 cannot make the ship stop completely. However,

the torque of the propeller eventually becomes 0, after several reasonable decreases.

From the change of the curve illustrated in Figure 11, it can be seen that the simulation model established is accurate and in line with the actual situation. Therefore, when the actual ship stops sailing, the measure taken is to rotate the propeller in the opposite direction for a period of time to make the ship's speed drop to a small enough level, and then stop the propulsion motor.

4. Conclusion

In this paper, the simulation technology of mechanical load is studied, based on the torque characteristics of typical mechanical load. The control strategy of MRASO-MPTC is designed by using PMSM as the load simulation motor. The MRASO sensorless method is used to replace the traditional mechanical sensor, and the MC drive mode is used to propose the MPTC strategy. MC is used to replace the conventional AC-DC-AC converter, and MPTC is used to select the optimal voltage space vector to make the system have good torque and flux control effect. The simulation results show that the MRASO-MPTC strategy can make the MC-driven PMSM simulation system run stably and has a good control effect.

From the simulation presented in the present paper, it can also be concluded that, in addition to the special emergency situation, the start and stop of the ship generally adopts the graded acceleration and deceleration way, which can avoid the overload of the propeller shaft and damage to the propulsion motor, which, in its turn, has guideline significance for the operation of the real ship. The simulation results can also provide reference for building ship motion model and load motor control, when developing electric propulsion simulator.

REFERENCES

Wang, K., Li, H., Li, H. & Gao, J. (2023) Error Model and Forecasting Method for Electronic Current Transformers Based on LSTM. *Tehnički Vjesnik [Technical Gazette]*. 30(2), 399-407. doi: 10.17559/TV-20221109032034.

Oral, A. E. & Akay, O. E. (2022) Prediction of Vibration in the Discharge Ring of a River Type Hydroelectric Power Plant with Bulb Turbine Using Artificial Neural Networks and Support Vector Machine. *Tehnički Vjesnik [Technical Gazette]*. 29(5), 1726-1732. doi: 10.17559/TV-20210906114213.

Taghinezhad Vaskeh Mahaleh, A. M., Ghanbari, M. & Ebrahimi, R. (2024) A novel vector control strategy for sensorless 3φ induction machines under single-phase fault. *IET Power Electronics*. 17(3), 422-437. doi: 10.1049/pel2.12653.

Kulikova, M. V. & Kulikov, G. Y. (2024) Continuous–discrete derivative-free extended Kalman filter based on Euler–Maruyama and Itô–Taylor discretizations: Conventional and square-root implementations. *European Journal of Control*. 76, 100960. doi: 10.1016/j.ejcon.2024.100960.

Tomov, M., Gecevska, V. & Vasileska, E. (2022) Modelling of multiple surface roughness parameters during hard turning: A comparative study between the kinematical-geometrical copying approach and the design of experiments method (DOE). *Advances in Production Engineering & Management*. 17(1), 75-88. doi: 10.14743/apem2022.1.422.

Espinoza Fraire, T., Saenz, A., Gandarilla, I. & Giernacki, W. (2024) MRAS Using Lyapunov Theory with Sliding Modes for a Fixed-Wing MAV. *Applied Sciences*. 14(5), 2198. doi: 10.3390/app14052198.

Agyeman, B. T., Nouri, M., Appels, W. M., Liu, J. & Shah, S. L. (2024) Learning-based multi-agent MPC for irrigation scheduling. *Control Engineering Practice*. 147, 105908. doi: 10.1016/j.conengprac.2024.105908

Liu, J. D., Chen, J. Q., Wu, Y. Q., Han, F. & Guan, Y. F. (2023) Simulation Method for Stitch Wire Vibration Load and Fatigue Life. *International Journal of Simulation Modelling*. 22(4), 643-654. doi: 10.2507/IJSIMM22-4-664.

Tarbajovsky, P., Puskar, M. & Sabadka D. (2023) Simulation Model of Vehicle Emission Reduction Exhaust System. *International Journal of Simulation Modelling*. 22(4), 679-689. doi: 10.2507/IJSIMM22-4-675.

Popovici, A. T. & Onea, A. (2021) Generalized Differential Mathematical Model in Stator Reference Frame for PMSM and VRSM Simulation. Bulletin of the Polytechnic Institute of Iaşi. *Electrical Engineering, Power Engineering, Electronics Section*. 67(4), 43-55. doi: 10.2478/bipie-2021-0021.

Saihi, L., Berbaoui, B., Ferroudji, F., Bakou, Y. & Benfriha, E. (2023) Robust sensor-less sliding mode of second-order control of doubly fed induction generators in variable speed wind turbine systems based on a novel MRAS-ANFIS observer. *Wind Engineering*. 47(4), 766-782. doi: 10.1177/0309524X231158707.

Nikitin, A. Y., Zvereva, T. V., Verzhutskaya, Y. A., Lyapunov, A. V., Rudakov, D. M., Kolesnikova, V. Y. Gordeiko, N. S. & Andaev, E. I. (2023) Fauna and Abundance of Ixodid Ticks and Their Infection with Human Pathogens on Popov Island, Primorskii Territory. *Entomological Review*. 103(4), 485-491. doi: 10.1134/S0013873823040097.

Esquível, M. L. & Krasii, N. P. (2020) Examples of financial market models obtained by Euler discretization of continuous models. *Global and Stochastic Analysis*. 7(1), 35-53.

Arshad, M. H., Raja, M. M. & Zhao, Q. (2023) Neutral Point Voltage Balancing Using MOPSO based Weighting Factor Tuning for FCS-MPTC of Three Level T-Type VSI Fed IM Drive. *IFAC PapersOnLine*. 56(2), 435-440. doi: 10.1016/j.ifacol.2023.10.1606.

Riaz, A., Xingong, L., Jiao Z. & Shahbaz, M. (2023) Dynamic volatility spillover between oil and marine shipping industry. *Energy Reports*. 9(5), 3493-3507. doi: 10.1016/j.egyr.2023.02.025.